experiment and computation are attributed to the normal coordinate analysis (harmonic approximation) applied to the highly anharmonic S_1 PES.

We thus achieved direct experimental tracking of the continuous structural evolution of a reacting polyatomic molecule by monitoring the evolving frequency of a spectator wave packet. The spectator frequency showed a gradual downshift over the course of the isomerization through a large anharmonic coupling to the isomerization coordinate. This observation arises from the gradual twisting of the olefinic moiety, realized by the out-of-plane motion of the two ethylenic hydrogens with minimal change in the molecular volume. The global molecular rearrangements visualized here lead to the structure at the S_1/S_0 conical intersection, which may be accompanied with further pyramidalization of one ethylenic carbon (*19*). Femtosecond time-domain Raman spectroscopy offers effective probing of complicated multidimensional RC of polyatomic molecules that cannot be tracked by conventional vibrational spectroscopy.

References and Notes

1. M. D. Fayer, *Ultrafast Infrared and Raman Spectroscopy* (Marcel Dekker, New York, 2001).
2. J. Herbst, K. Heyne, R. Diller, *Science* **297**, 822 (2002).
3. P. Kukura, D. W. McCamant, R. A. Mathies, *Annu. Rev. Phys. Chem.* **58**, 461 (2007).
4. P. Kukura, D. W. McCamant, S. Yoon, D. B. Wandschneider, R. A. Mathies, *Science* **310**, 1006 (2005).
5. U. Banin, S. Ruhman, *J. Chem. Phys.* **99**, 9318 (1993).
6. S. Fujiyoshi, S. Takeuchi, T. Tahara, *J. Phys. Chem. A* **107**, 494 (2003).
7. Materials and methods are available as supporting online material on *Science* Online.
8. G. Cerullo *et al.*, *J. Phys. Chem. A* **107**, 8339 (2003).
9. T. Hornung, H. Skenderovic, M. Motzkus, *Chem. Phys. Lett.* **402**, 283 (2005).
10. M. Sumitani, N. Nakashima, K. Yoshihara, *Chem. Phys. Lett.* **68**, 255 (1979).
11. S. Abrash, S. Repinec, R. M. Hochstrasser, *J. Chem. Phys.* **93**, 1041 (1990).
12. D. C. Todd *et al.*, *J. Chem. Phys.* **93**, 8658 (1990).
13. S. T. Repinec, R. J. Sension, A. Z. Szarka, R. M. Hochstrasser, *J. Phys. Chem.* **95**, 10380 (1991).
14. R. J. Sension, A. Z. Szarka, R. M. Hochstrasser, *J. Chem. Phys.* **97**, 5239 (1992).
15. D. C. Todd, G. R. Fleming, *J. Chem. Phys.* **98**, 269 (1993).
16. J. Saltiel, *J. Am. Chem. Soc.* **90**, 6394 (1968).
17. A. B. Myers, R. A. Mathies, *J. Chem. Phys.* **81**, 1552 (1984).
18. H. Petek *et al.*, *J. Phys. Chem.* **94**, 7539 (1990).
19. J. Quenneville, T. J. Martinez, *J. Phys. Chem. A* **107**, 829 (2003).
20. J. M. Rodier, A. B. Myers, *J. Am. Chem. Soc.* **115**, 10791 (1993).
21. The first component is due to instantaneous electronic response of S_1 *cis*-stilbene. The second 70-fs decay corresponds to the $S_n \rightarrow S_1$ internal conversion that occurs after the $S_n \leftarrow S_1$ excitation by the P_2 pulse. The third component decays with the S_1 lifetime. The appearance of this long-lasting component suggests that a fraction of the S_n molecules does not go back to the S_1 state but follows other relaxation routes (permanent bleaching) (*6*).
22. W. M. Kwok *et al.*, *J. Raman Spectrosc.* **34**, 886 (2003).
23. K. Ishii, S. Takeuchi, T. Tahara, *Chem. Phys. Lett.* **398**, 400 (2004).
24. The initial frequency was obtained by the linear fit as the intercept at zero delay, and it was separately evaluated as 243.1 ± 2.3 cm^{-1} in hexadecane and 241.1 ± 1.6 cm^{-1} in methanol. On the average, we determined the common initial frequency as 242 ± 2 cm^{-1}.
25. We made Fourier transform analysis of a beating feature observed in the $S_n \leftarrow S_1$ transient absorption and obtained its power spectrum that shows an intense band corresponding to the 240-cm^{-1} vibration. The center-of-mass frequency of the band was evaluated as 231 ± 3 cm^{-1} in both cyclohexane and methanol.
26. S. Pedersen, L. Banares, A. H. Zewail, *J. Chem. Phys.* **97**, 8801 (1992).
27. H. Iikura, T. Tsuneda, T. Yanai, K. Hirao, *J. Chem. Phys.* **115**, 3540 (2001).
28. R. Improta, F. Santoro, *J. Phys. Chem. A* **109**, 10058 (2005).
29. As already reported, the 240-cm^{-1} vibration exhibits a high Franck-Condon activity in the $S_1 \leftarrow S_0$ transition, indicating that it is a totally symmetric, Raman-active mode showing a large S_0/S_1 potential displacement (*23*). Among the totally symmetric candidate modes in Fig. 4D (ν_{32}, ν_{33}, ν_{34}), the initial frequencies of the ν_{33} and ν_{34} modes are close to 240 cm^{-1}. We found that the S_1/S_0 potential displacement along the ν_{33} mode is largest: Absolute potential gradients at $s = 0$, which reflect the potential displacement, were calculated as 0.0036 (ν_{32}), 0.0076 (ν_{33}), and 0.0033 (ν_{34}) hartree/(bohr·amu$^{1/2}$), respectively (where amu stands for atomic mass unit). Therefore, we assigned the ν_{33} mode to the 240-cm^{-1} vibration observed experimentally.
30. K. Iwata, H. Hamaguchi, *J. Phys. Chem. A* **101**, 632 (1997).

31. This work was supported in part by Grant-in-Aid for Science Research on Priority Area (no. 19056009) from the Ministry of Education, Culture, Sports, Science, and Technology of Japan. S.T. acknowledges financial support by a Grant-in-Aid for Scientific Research (B) (no. 19350017) from the Japan Society for the Promotion of Science (JSPS). T. Tahara and S.R. acknowledge the JSPS invitation fellowship program.

Supporting Online Material

www.sciencemag.org/cgi/content/full/322/5904/1073/DC1
Materials and Methods
References

23 May 2008; accepted 15 September 2008
10.1126/science.1160902

Random Tiling and Topological Defects in a Two-Dimensional Molecular Network

Matthew O. Blunt,[1] James C. Russell,[1] María del Carmen Giménez-López,[2] Juan P. Garrahan,[1] Xiang Lin,[2] Martin Schröder,[2] Neil R. Champness,[2]* Peter H. Beton[1]*

A molecular network that exhibits critical correlations in the spatial order that is characteristic of a random, entropically stabilized, rhombus tiling is described. Specifically, we report a random tiling formed in a two-dimensional molecular network of *p*-terphenyl-3,5,3′,5′-tetracarboxylic acid adsorbed on graphite. The network is stabilized by hexagonal junctions of three, four, five, or six molecules and may be mapped onto a rhombus tiling in which an ordered array of vertices is embedded within a nonperiodic framework with spatial fluctuations in a local order characteristic of an entropically stabilized phase. We identified a topological defect that can propagate through the network, giving rise to a local reordering of molecular tiles and thus to transitions between quasi-degenerate local minima of a complex energy landscape. We draw parallels between the molecular tiling and dynamically arrested systems, such as glasses.

The tiling of surfaces with simple polygons has fascinated scientists, mathematicians, and artists in both ancient and modern cultures. The mathematical rules that govern the formation of periodic tilings, in which tiles are regularly placed on a surface, have been extensively studied and provide the foundation for the classification of crystalline materials. More recently, the discovery of quasi-crystals has inspired great interest in aperiodic tilings, which exhibit symmetries that are not compatible with translational order (*1*–*5*). It is also possible to form tilings in which translational symmetry is absent by using simple tile shapes such as the rhombus with internal angles of 60° and 120°. Rhombus, or lozenge, tilings lead to a particularly rich range of arrangements, which may be periodic, but random nonperiodic tilings are also permitted (*6*, *7*) and have attracted great interest because of their relevance to mixing algorithms (*8*, *9*), antiferromagnetism (*10*, *11*), and entropic models of quasi-crystals (*12*–*15*).

We show that a rhombus tiling may be realized experimentally in a two-dimensional arrangement of organic molecules adsorbed on graphite. Specifically, we studied the molecule *p*-terphenyl-3,5,3′,5′ -tetracarboxylic acid (TPTC) (Fig. 1A), which was synthesized as described in (*16*). The choice of molecule was motivated by the placement of carboxylic acid groups that promote directional intermolecular hydrogen bonding. For TPTC, these groups stabilize two possible relative placements of neighboring molecules, which we refer to as the parallel (Fig. 1B) and arrowhead (Fig. 1C) configurations. Small quantities of a saturated solution of TPTC in nonanoic acid were applied to a freshly cleaved highly oriented pyro-

[1]School of Physics and Astronomy, University of Nottingham, University Park, Nottingham NG7 2RD, UK. [2]School of Chemistry, University of Nottingham, University Park, Nottingham NG7 2RD, UK.

*To whom correspondence should be addressed. E-mail: neil.champness@nottingham.ac.uk (N.R.C.); peter.beton@nottingham.ac.uk (P.H.B.)

lytic graphite (HOPG) substrate, and images of the interface between HOPG and the TPTC solution were acquired by using a scanning tunneling microscope (STM) [see (*16*) for full experimental details]. The samples were prepared and imaged at room temperature. Nonanoic acid has been identified as a suitable solvent by Lackinger *et al.* (*17*, *18*) in their investigations of trimesic and related acids, and the properties of molecular networks stabilized by noncovalent interactions such as hydrogen bonding have been reviewed by a number of authors (*19*–*21*). There have also been recent studies of molecules functionalized with multiple carboxylic acid groups, similar to TPTC (*22*–*24*).

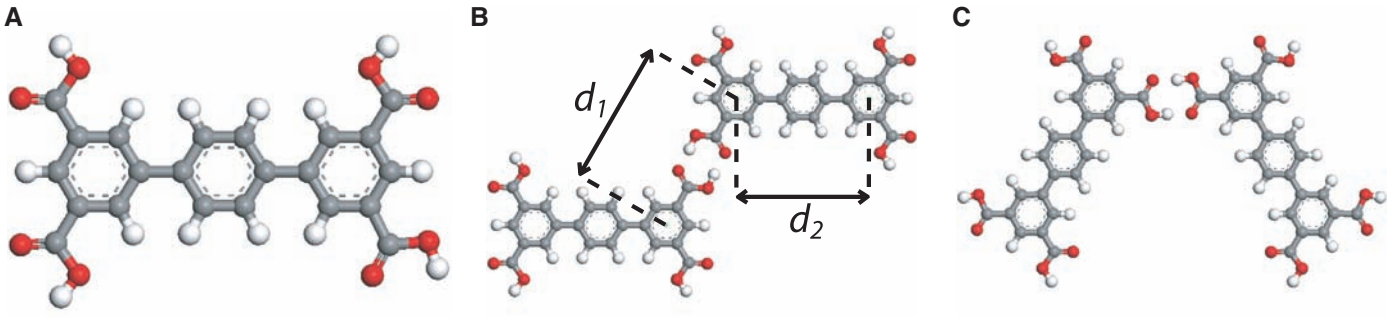

Fig. 1. (**A**) Molecular structure of TPTC. Two possible arrangements for a pair of TPTC molecules linked via a carboxylic acid–carboxylic acid hydrogen bond, (**B**) with the long axes of both molecules parallel to each other, and (**C**) with one molecule rotated by 60° with respect to the other. Marked on (B) are the calculated distances (*16*) between two phenyl rings of different TPTC molecules taken across a carboxylic–carboxylic hydrogen bond (d_1), and the distance between the two end phenyl rings of a single TPTC molecule (d_2).

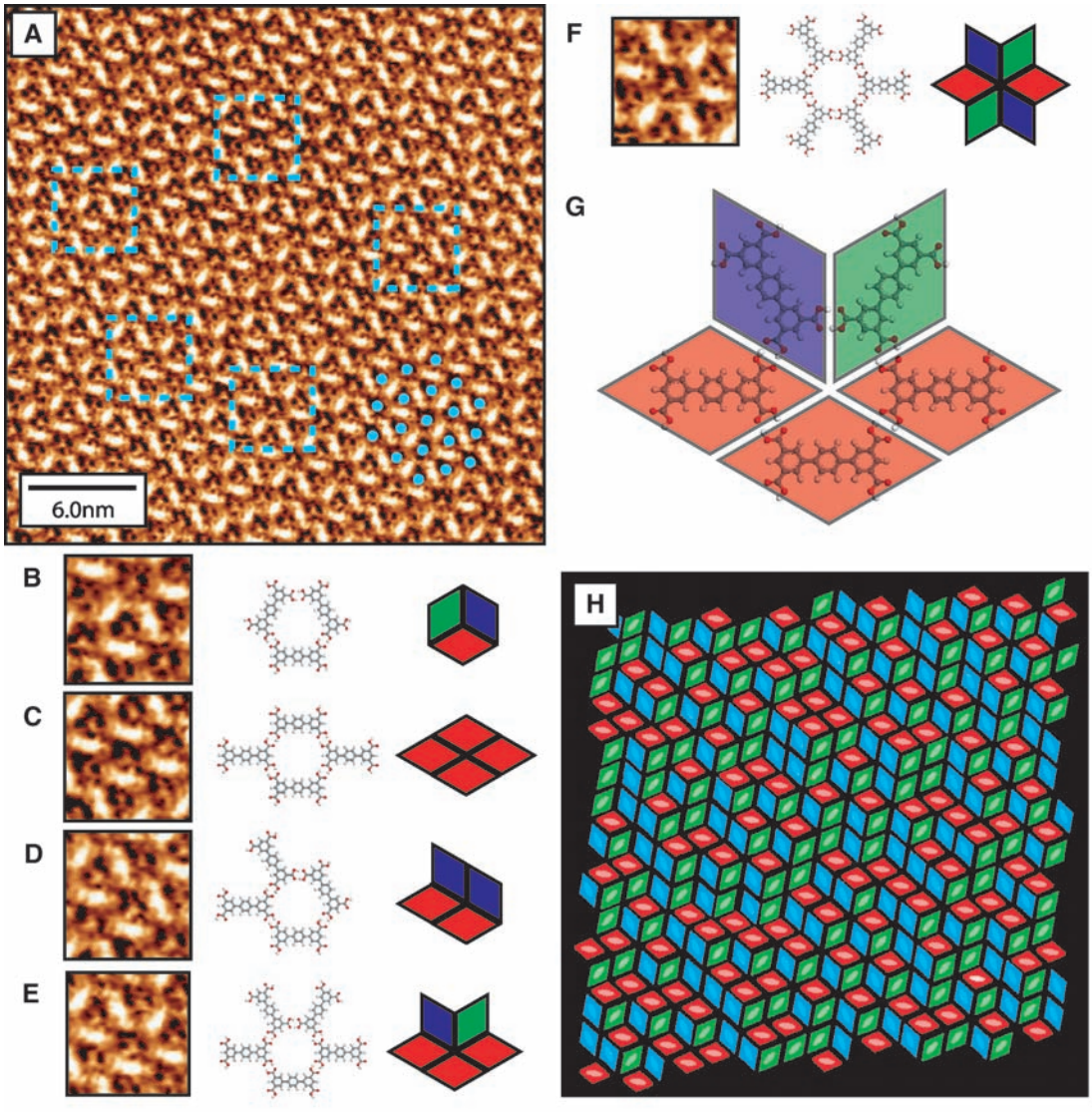

Fig. 2. (**A**) STM image of a typical area of TPTC network at the nonanoic acid/HOPG interface. The group of three phenyl rings constituting the backbone of the TPTC molecules appear as bright rodlike features in the image. The hexagonal orientational order of the structure is highlighted by the group of blue dots in the lower right-hand corner of the image, marking the location of dark contrast regions in the image (depressions/pores in the network). (**B** to **F**) Molecular ball and stick diagrams and tiling representations for the five possible arrangements of TPTC molecules around a network pore. Also shown are magnified STM image examples of each pore type from (A); the locations of the magnified regions are marked in (A) by blue dashed squares. Scanning conditions of (A) were tunneling current (I_t) = 0.015 nA and tip voltage (V_t) = 1200 mV. (**G**) Enlarged version of the molecular arrangement shown in (E). The equivalent tiling representation is shown as a transparent overlay, which highlights the location of the carboxylic acid–carboxylic acid hydrogen bonds at the midpoint of edges between tiles. (**H**) Corresponding tiling representation of (A). The coloration of (H) represents the three possible orientations of rhombi within the tiling (red, green, and blue). Idealized representations of the molecular positions are shown faintly in the tiling.

A typical area of the TPTC network adsorbed on the HOPG surface is shown in Fig. 2A. The terphenyl backbones of the molecules appear as bright rodlike features, and the molecular arrangement is unusual because it exhibits hexagonal orientational order but no translational symmetry. The hexagonal order may be discerned from the array of blue dots overlaid on dark contrast features (corresponding to depressions or pores) in Fig. 2A and, using calibration scans of the graphite substrate, we found that the hexagonal array has a period of 16.6 ± 0.8 Å oriented at an angle of ±6° to the HOPG substrate (*16*). Although the pores are regularly arranged, the molecular network enclosing them is not translationally ordered. Figure 2, B to F, shows that the molecular arrangements enclosing different pores (highlighted areas in Fig. 1A) are hexagons formed by a varying number of molecules.

For example, Fig. 2B shows a hexagon formed by three molecules with edges that alternate between a terphenyl backbone and a carboxylic acid–carboxylic acid junction. Figure 2, C and D, shows two alternative hexagonal arrangements formed by the junction of four molecules with two edges formed by the terphenyl backbone. Similarly, the junction in Fig. 2E is formed by five molecules with one terphenyl edge, and the junction in Fig. 2F is formed by six molecules with no terphenyl edges. The lengths of the hydrogen-bonded and terphenyl edges (equivalent to d_1 and d_2 as defined in Fig. 1B) are calculated to be 9.6 and 8.7 Å [the intermolecular binding energy $E_{HB} = 0.80$ eV is calculated to be the same for the parallel and arrowhead arrangements (*16*)], giving estimated widths of the hexagons in Fig. 2 ranging from 15.8 Å (Fig. 2B) to 16.6 Å (Fig. 2F), which is in good agreement with the measured periodicity. The molecular array shown in Fig. 2A may be built by combining these five structural units in an arrangement that exhibits orientational symmetry but no translational order.

The network may be mapped onto a tiling by replacing each molecule with a rhombus [see (*25*) for another example linking molecular arrays to tiling problems]. Each molecule in the network points along one of three high-symmetry directions, and we have chosen, for clarity, to represent these three molecular orientations as rhombi with different colors. To illustrate the tiling, we have converted each of the hexagonal structural units discussed above into rhombi (Fig. 2). The representations of the junctions in Fig. 2, B to F, correspond to vertices where three, four, five, or six rhombi meet. These diagrams also show that, at a molecular level, the mapping is possible because the intermolecular bonds between neighboring molecules are located at the midpoint of the rhombus edges (Fig. 2G). We suggest that this symmetry is key to identifying other candidate molecules that might form similar networks.

The molecular network displayed in Fig. 2A can be mapped into rhombi, and the resultant tiling is shown in Fig. 2H. The mapping directly accounts for the presence of orientational symmetry combined with an absence of translational order because the rhombus vertices (pores in the STM images) fall on a hexagonal lattice, even though the arrangement of rhombi is not ordered. Thus, we demonstrate that the molecular array is equivalent to a rhombus tiling.

We also observed tiling defects in the form of triangular voids enclosed completely by rhombi (Fig. 3). These voids are topological defects that occur in two states of effective "charge" corresponding to triangles pointing either "up" or "down" and have been considered theoretically but have not previously been observed (*26*–*28*). We observed ~3×10^{-3} defects per adsorbed molecule and may unequivocally distinguish these voids from other less intrinsically interesting defects, such as vacancies. The triangular defects have been observed to propagate through the network, as shown in Fig. 3, C to H. This movement results in a rearrangement of a single molecule (or tile) within the network. Figure 3, C and F, shows a comparison of images before and after such a transition, in which, as expected, effective charge is conserved. The triangular defect undergoes a second movement between Fig. 3, E and G. In our images, this transition appears to be mediated by the temporary presence of an additional species at the defect site, as highlighted in Fig. 3, C and E, possibly an additional TPTC molecule temporarily bound by hydrogen bonding. Although it is difficult to determine the exact details of the atomistic mechanism for defect movement, this sequence of images shows that defect propagation through the network gives rise to a reordering of molecular tiles and facilitates a transition between different local energy minima.

To determine whether the observed rhombus tilings are ordered or random, we followed previous theoretical studies (*10*, *12*) and introduced an effective height $h(x,y)$ at each vertex (x,y). The height was calculated with the scheme shown in Fig. 4A, in which a displacement along a rhombus edge leads to a change in height of ±1. By arbitrarily choosing an origin with zero height, it is possible to define $h(x,y)$ for all vertices of a perfect (defect-free) tiling. Within this scheme, a tiling may be visually considered as a perspective of the surface of a simple cubic lattice when viewed along a (111) direction. More formally, the rhombus tiling is equivalent to the projection of an irregular surface of a three-dimensional simple cubic crystal onto a (111) plane of the cubic lattice. A map of effective height of the STM image (Fig. 2A) is shown in Fig. 4C.

Within the random tiling hypothesis (*11*), the tilings may be analyzed by introducing an effective free energy G, which, assuming that all vertex types (shown in Fig. 2) are degenerate, is determined entirely by an entropic contribution and is given by $G = (K_o/2)\int|\nabla h|^2\, dxdy$. This contribution is equivalent to the energy of a deformed surface with elastic constant K_o. The gradient ∇h corresponds to the projection in the (x,y) plane of the normal to the representative surface. The tilings that are generated by this free energy have a height representation for which $\langle \nabla h \rangle = 0$, that is, a surface which on average is flat and par-

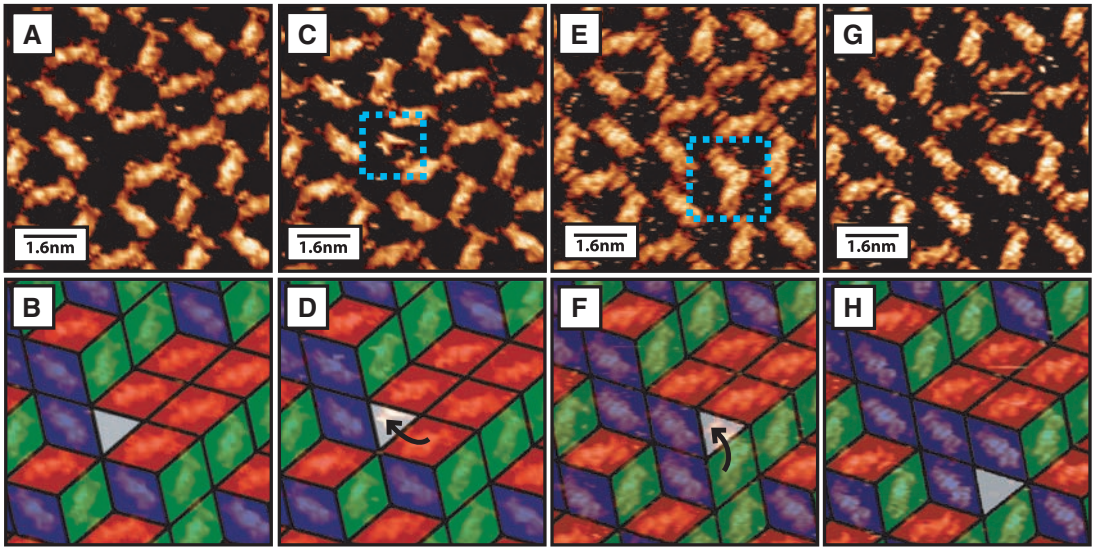

Fig. 3. (**A**, **C**, **E**, and **G**) STM images showing two separate movements of a single defect through the network structure. (**B**, **D**, **F**, and **H**) Tiling representation of the network structure during the defect motion. The effective rearrangements of rhombi in the tiling are marked by the black arrows in (D) and (F). Transient image artifacts observed within the defect site before defect motion are highlighted by blue dashed squares [(C) and (E)]. Scanning conditions for all images were I_t = 0.021 nA and V_t = 1200 mV.

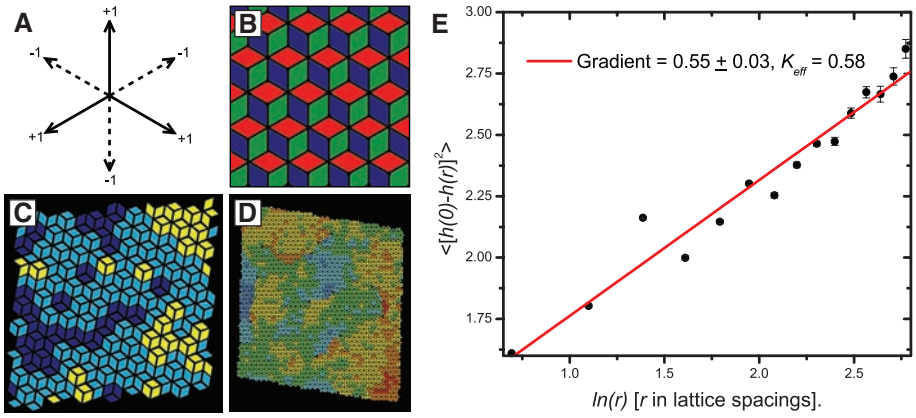

Fig. 4. (**A**) Scheme for evaluating height function of a tiling. A displacement from a vertex along three of the possible directions leads to an increase in height by 1 as shown; a displacement along the other three directions leads to a decrease by 1. (**B**) A schematic showing a flat undeformed representative surface to be compared with the (111) surface of a simple cubic crystal. (**C**) Height representation of tiling in Fig. 2. Here the height of a tile is calculated as the average over its four vertices; different heights are represented as different colors. (**D**) Height map of one of the large area scans (100 nm by 100 nm) used to generate correlation function [see (*16*) for more details]. (**E**) Dependence of correlation on separation demonstrating logarithmic dependence. Scanning conditions for all images were I_t = 0.015 nA and V_t = 1200 mV.

allel to a (111) plane of the projected cubic lattice, which is equivalent to a requirement that equal numbers of tiles are oriented in each of the three possible directions. Fluctuations in height with wavevector $\underline{k}$ are expected with a Fourier spectrum $h(\underline{k}) \propto K_o^{-1}|\underline{k}|^{-2}$. In two dimensions, this spectrum leads to logarithmic spatial correlations in $h(x,y)$, $C(r) = \langle[h(0) - h(r)]^2\rangle = (\pi K_o)^{-1} \ln(r) + c$, where c is a constant and, for the maximally random rhombus tiling, $K_o = \pi/9$ (*10*, *12*).

We calculated the height correlation function $C(r)$ from STM images that had been converted to a height representation (Fig. 4D). The fraction of tiles pointing in the three directions is in the ratio 1:1:1, within statistical error, and thus the condition $\langle\nabla h\rangle = 0$ is satisfied [see (*16*) for tile maps and ratios of tile orientations]. It is not possible to solely specify $h(x,y)$ in the presence of triangular void defects because the line integral of $h(x,y)$ along a closed path around a triangular void gives a nonzero value corresponding to the winding number of the defect (in this case, ±3). However, it is possible to unambiguously calculate the contributions to the height correlation function in regions that do not enclose defects. Our method for calculating $C(r)$ is based on this approach and provides reliable data for $r \leq r_d$, the average defect separation.

As shown in Fig. 4E, the measured $C(r)$ has the expected logarithmic dependence on r, corresponding to the critical correlations of a random rhombus tiling (*12*). The effective elasticity of the tiling may be extracted from the prefactor of the logarithm. We find $K_{eff} = 0.58 \pm 0.03$, or equivalently $K_{eff}/K_o \sim 1.7$.

The enhancement of the elastic constant over the expected value K_o is explained as a breaking of the exact degeneracy in local bonding arrangements, with a small energetic preference for the arrowhead (Fig. 1C) configuration. This difference in energy results in an energy cost for vertices that have neighboring tiles in the parallel configuration (Fig. 2, C to E). These vertices [which are not present on the idealized undeformed (111) representative surface, for which molecules are exclusively in the arrowhead arrangement (Fig. 4B)] are associated with local changes in height $\nabla h \neq 0$, leading to an energetic contribution to the free energy in addition to the purely entropic term discussed above. These effects lead to an increase in the effective elastic constant K_{eff} in G.

This explanation is consistent with results by Alet *et al.* (*29*) for closed packed dimers on the square lattice with aligning interactions, in which there is a critical phase with an effective elasticity that increases with increasing interaction strength Δ [and an eventual phase transition to an ordered phase for $\Delta \sim kT$ (T, temperature), where other terms become relevant in the free energy G (*29*)]. In the context of our experiments, Δ characterizes the energy difference between the parallel and arrowhead configurations. Our finding of logarithmic correlations with K_{eff} close to K_o, to within a factor 2, confirms that our system is in the random tiling regime and therefore $\Delta < kT$ (0.03 eV). This very small value of energy, comparable with the uncertainty in our calculation of E_{HB}, highlights the delicate balance required for entropically stabilized randomness in the rhombus tiling.

Although the above analysis of the spatial distribution of tiles is based on the equilibrium free energy G, it is clear that the tilings are frozen, with minimal temporal evolution, in one local minimum of a complex energy landscape. The system is dynamically arrested, similar to a glass, and all tile movements are activated with an energy cost that is expected to scale with the number of intermolecular hydrogen bonds that must be broken. Triangular defects, which mediate the only tile rearrangements that have been experimentally observed, have the lowest activation barrier because only three bonds must be broken in order to move a molecule directly adjacent to a defect. Other tile rearrangements, such as the 60° rotation of the hexagonal unit in Fig. 2B, often considered in the context of mixing algorithms for perfect (defect-free) random tilings (*8*), require six bonds to be broken and would be expected to be exponentially suppressed. The observation of the propagation of localized defects as a mechanism for transitions between different local energy minima is highly reminiscent of dynamically facilitated models of glass formers (*30*, *31*). Our results demonstrate the potential of molecular tilings as model systems for the study of glasses and provide an interesting alternative to the random molecular networks recently identified by Otero *et al.* as glassy systems (*32*).

Our results show that, once formed, tilings are trapped in one of a large number of quasi-degenerate locally stable states that can rearrange through defect migration. Overall, the connection between rhombus tiling and molecular architecture, through the approximate equality $d_1 \sim d_2$, leads to design rules for a general class of analogous molecular networks in two and three dimensions that can provide novel model systems for the study of random structural arrangements and dynamically arrested materials.

References and Notes

1. D. Shechtman, I. Blech, G. Gratias, J. W. Cahn, *Phys. Rev. Lett.* **53**, 1951 (1984).
2. D. Levine, P. J. Steinhardt, *Phys. Rev. Lett.* **53**, 2477 (1984).
3. G. Onoda, P. J. Steinhardt, D. J. DiVincenzo, J. E. S. Socolar, *Phys. Rev. Lett.* **60**, 2653 (1988).
4. J. Ledieu *et al.*, *Phys. Rev. Lett.* **92**, 135507 (2004).
5. J. Yuhara *et al.*, *Phys. Rev. B* **70**, 024203 (2004).
6. M. E. Fisher, *Phys. Rev.* **124**, 1664 (1961).
7. P. Kasteleyn, *J. Math. Phys.* **4**, 287 (1963).
8. D. B. Wilson, *Ann. Appl. Probab.* **14**, 274 (2004).
9. H. Cohn, R. Kenyon, J. Propp, *J. Am. Math. Soc.* **14**, 297 (2001).
10. H. W. J. Blote, H. J. Hilhorst, *J. Phys. A* **15**, L631 (1982).
11. R. Moessner, S. L. Sondhi, E. Fradkin, *Phys. Rev. B* **65**, 024504 (2002).
12. C. L. Henley, in *Quasicrystals, the State of the Art*, D. P. DiVencenzo, P. J. Steinhardt, Eds. (World Scientific, Singapore, 1999), p. 459.
13. M. Widom, D. P. Deng, C. L. Henley, *Phys. Rev. Lett.* **63**, 310 (1989).
14. N. Destainville, *Phys. Rev. Lett.* **88**, 030601 (2002).
15. A. S. Keys, S. C. Glotzer, *Phys. Rev. Lett.* **99**, 235503 (2007).
16. Materials and methods and additional data are available as supporting material on *Science* Online.
17. M. Lackinger, S. Griessl, W. A. Heckl, M. Hietschold, G. W. Flynn, *Langmuir* **21**, 4984 (2005).
18. S. J. H. Griessl *et al.*, *Langmuir* **20**, 9403 (2004).
19. S. de Feyter, F. C. de Schryver, *J. Phys. Chem. B* **109**, 4290 (2005).
20. J. V. Barth, G. Costantini, K. Kern, *Nature* **437**, 671 (2005).
21. F. Rosei *et al.*, *Prog. Surf. Sci.* **71**, 95 (2003).
22. H. Zhou *et al.*, *J. Am. Chem. Soc.* **129**, 13774 (2007).
23. M. Blunt *et al.*, *Chem. Commun.* 2304 (2008).
24. M. Li *et al.*, *Angew. Chem. Int. Ed.* **47**, 6717 (2008).
25. M. Pivetta, M. C. Blum, F. Patthey, W. D. Schneider, *Angew. Chem. Int. Ed.* **47**, 1076 (2008).
26. M. E. Fisher, J. Stephenson, *Phys. Rev.* **132**, 1411 (1963).

27. J. Linde, C. Moore, M. G. Nordahl, *Discrete Mathematics and Theoretical Computer Science Proceedings AA* (DM-CCG) *23* (2001).
28. W. Krauth, R. Moessner, *Phys. Rev. B* **67**, 064503 (2003).
29. F. Alet *et al.*, *Phys. Rev. Lett.* **94**, 235702 (2005).
30. G. H. Fredrickson, H. C. Andersen, *Phys. Rev. Lett.* **53**, 1244 (1984).
31. J. P. Garrahan, D. Chandler, *Proc. Natl. Acad. Sci. U.S.A.* **100**, 9710 (2003).
32. R. Otero *et al.*, *Science* **319**, 312 (2008).
33. We thank the UK Engineering and Physical Sciences Research Council (EPSRC) for financial support under grant EP/D048761/01. J.P.G. was supported by EPSRC grant GR/S54074/01. M.S. acknowledges receipt of a Royal Society Wolfson Merit Award.

Supporting Online Material
www.sciencemag.org/cgi/content/full/322/5904/1077/DC1
Materials and Methods
Figs. S1 to S4
References

16 July 2008; accepted 6 October 2008
10.1126/science.1163338

Observing the Creation of Electronic Feshbach Resonances in Soft X-ray–Induced O_2 Dissociation

Arvinder S. Sandhu,[1]*† Etienne Gagnon,[1]* Robin Santra,[2,3] Vandana Sharma,[1] Wen Li,[1] Phay Ho,[2] Predrag Ranitovic,[4] C. Lewis Cocke,[4] Margaret M. Murnane,[1]‡ Henry C. Kapteyn[1]

When an atom or molecule is ionized by an x-ray, highly excited states can be created that then decay, or autoionize, by ejecting a second electron from the ion. We found that autoionization after soft x-ray photoionization of molecular oxygen follows a complex multistep process. By interrupting the autoionization process with a short laser pulse, we showed that autoionization cannot occur until the internuclear separation of the fragments is greater than approximately 30 angstroms. As the ion and excited neutral atom separated, we directly observed the transformation of electronically bound states of the molecular ion into Feshbach resonances of the neutral oxygen atom that are characterized by both positive and negative binding energies. States with negative binding energies have not previously been predicted or observed in neutral atoms.

The ability to reveal fast correlated electronic dynamics with ultrafast x-rays has attracted considerable interest in recent years. In general, some of the fastest electronic processes involve highly excited states. Autoionization after photoionization of an electron from an atom, molecule, or solid is a good example of one such process (*1*–*8*). Autoionization is an important electronic many-body problem in molecules, and the electrons and ions produced also contribute to radiation damage in materials and biological systems (*9*). In the autoionization of a deep inner-shell hole, an electron from a higher energy level fills the hole, while a second outer (Auger) electron is ejected, carrying away excess energy. Auger decay from a deep inner-shell hole is always energetically allowed, both in isolated atoms and molecules. In this case, the molecular environment generally plays a minor role. In contrast, autoionization of an inner-valence vacancy in an isolated atom is often energetically forbidden. For example, the $2s^1 2p^4\ ^2P$ inner-valence state of O^+ lies 40 eV above the ground state of atomic oxygen but 9 eV below the O^{2+} ground state and can therefore only decay radiatively; that is, by emitting a photon. However, in polyatomic systems, autoionization after inner-valence ionization can be energetically allowed because the molecular environment can play a role. Because the two final-state charges in a molecular dication do not have to sit on one atom, the Coulomb repulsion between the holes is reduced, and thus the double ionization threshold is lowered.

Interatomic Coulombic decay (ICD) in the Ne dimer, for instance, is a prominent example in which the molecular environment plays a major role in autoionization and has received much recent attention (*1*, *2*, *10*). In ICD in Ne, autoionization of a 2s hole relies on energy transfer between the two Ne atoms and thus preferentially takes place near the equilibrium separation of the atoms of the neutral Ne dimer. Molecular oxygen (O_2) can also autoionize after photoionization in the inner-valence region (*4*–*6*). However, O_2 does not follow the paradigm provided by ICD, in which autoionization occurs when the atoms are in proximity. Rather, Feifel *et al.* (*4*) performed a high-resolution coincident electron study of O_2 and concluded that the atomiclike character of the autoionization spectrum indicates that the decay takes place at large interatomic distances, which is in stark contrast to ICD. However, these experiments did not have any time resolution: Without the ability to observe intermediate states, it was not possible to uncover the mechanism for autoionization to fully understand what was happening.

In this work, we irradiated an O_2 molecule with a few-femtosecond x-ray pulse to create superexcited states of the O_2^+ molecular ion. We then used an ultrafast laser pulse to follow how this superexcited state evolves into an autoionizing state. We achieved this by interrupting the autoionization with an ultrafast laser pulse at different times during the process. First, we found that autoionization cannot occur until the molecular fragments are well-separated, by distances of >30 Å. Second, we found that the autoionizing state forms 300 fs after x-ray irradiation and emerges as a negative binding-energy Feshbach resonance. The use of ultrafast x-rays and lasers (*11*), in combination with a triple-coincidence detection scheme, allowed us to directly observe the onset of these negative binding-energy Feshbach autoionizing states. Before this work, the existence of negative binding-energy states in neutral atoms was not anticipated. Third, by providing an explanation for the atomic nature of the autoionization lines observed in O_2, we were able to highlight the dramatic difference between the roles of the molecular environment in ICD in van der Waals dimers and molecular autoionization, in which the presence of a molecular field can suppress, rather than enhance, autoionization. Finally, we showed that we can manipulate superheated, metastable, autoionizing states before they decay and actively influence, with a strong field, whether a superexcited state will have the opportunity to decay or not. This capability raises the possibility of coherent manipulation of highly excited quantum states, even when their energies lie above the ionization potential. Autoionization after soft x-ray photoionization of O_2 is thus a much more complex multi-step process than in the case of N_2, with which in recent studies we used an ultrafast soft x-ray pump combined with an infrared probe to study electron shakeup processes (*12*, *13*).

Several studies have reported the existence of negative binding energy states in multiply charged molecular ions (anions) (*14*–*16*). A particular electronic state is considered to have a negative binding energy when the kinetic energy of an ejected photoelectron is greater than the single-photon energy used for the ionization step. This means that the electronic state must be higher in energy than the ionization channel being considered. A state with negative binding energy must therefore be metastable. The repulsive Coulomb barrier in multiply charged anions supports long-lived shape resonances (metastable states that decay by tunneling through a potential barrier), which because of their long lifetime are easy to detect experimentally. To date, states with negative electron–binding energy were thought to be

[1]JILA, University of Colorado at Boulder, Boulder, CO 80309, USA. [2]Argonne National Laboratory, Argonne, IL 60439, USA. [3]Department of Physics, University of Chicago, Chicago, IL 60637, USA. [4]J. R. MacDonald Lab, Department of Physics, Kansas State University, Manhattan, KS 66506, USA.

*These authors contributed equally to this work.
†Present address: Department of Physics, University of Arizona, Tucson, AZ 85721–0081, USA.
‡To whom correspondence should be addressed. E-mail: margaret.murnane@colorado.edu